PERGAMON

International Journal of Heat and Mass Transfer 42 (1999) 1521–1534

International Journal of HEAT and MASS TRANSFER

Heat transfer in a three-dimensional turbulent boundary layer with longitudinal vortices

S.H. Lee, H.S. Ryou*, Y.K. Choi

Department of Mechanical Engineering, Chung-Ang University, 221 Heuksuk-Dong, Dongjak-Ku, Seoul, 156-756, South Korea

Received 20 September 1996; in final form 28 July 1997

Abstract

A numerical study of the heat transfer characteristics and turbulent structure is carried out in a three-dimensional turbulent boundary layer with longitudinal vortices. Longitudinal vortices are capable of strongly perturbing the turbulent and thermal boundary layer, which cause the anisotropy of turbulent intensities and augmentation of the heat transfer. This study uses a second-moment closure such as the Reynolds Stress Model (RSM) to capture the anisotropy of the turbulent structure effectively and the eddy-diffusivity model for predicting the thermal boundary layer. It can be concluded for turbulent flow that the RSM can produce the more accurate predictions for capturing the anisotropy than the standard k–ε model. Also, the results of heat transfer show that disturbing of the boundary layer causes the highest level of Stanton number in the region which the flows are directed toward the wall, but the vortices core is a region of relatively lower mixing. The eddy-diffusivity model for prediction of the thermal boundary layer can produce reasonably good agreement with the experimental data qualitatively. However, for more accurate prediction, it may be thought that the more elaborate model, such as the second-moment closure, for the turbulent-scalar-transport terms are required.

Nomenclature

B channel height
C_f skin friction coefficient ($= 2\tau_w/\rho U_\infty^2$)
c_μ, c_1, c_2 empirical constant
c_{w1}, c_{w2} empirical constant
$c_{\varepsilon 1}$, $c_{\varepsilon 2}$ empirical constant
c_P specific heat at constant pressure
d_{ij} diffusion tensor
k turbulent kinetic energy
l mixing length
n normal distance from the surface
P static pressure
P_{fn} Pee function
Pr Prandtl number
Pr_t turbulent Prandtl number
P_{ij} production tensor
$\dot{q}''_{app}$ apparent heat flux
$\dot{q}''_w$ wall heat flux [W m^{-2}]
$Re_{B/2}$ Reynolds number based on $B/2$ ($= \rho U_e B/(2\mu)$)
S_{ij} mean strain tensor
St local Stanton number
T temperature [°C]
T' fluctuating temperature
U_i time-mean velocity tensor (U, V, W in x-, y- and z-directions)
$\overline{u_i'u_j'}$ Reynolds stress tensor
u', v', w' axial, vertical, spanwise components of fluctuating velocity
W channel width.

Greek symbols

α_l, α_t thermal diffusivity and thermal eddy diffusivity respectively
ε dissipation rate of turbulent kinetic energy
ε_{ij} dissipation tensor
ϕ_{ij} pressure–strain correlation tensor
$\phi_{ij,1}$ pressure–strain correlation tensor (slow term)
$\phi_{ij,2}$ pressure–strain correlation tensor (rapid term)
$\phi_{ij,w}$ pressure–strain correlation tensor (wall-correction term)

* Corresponding author

0017–9310/98/$ - see front matter
PII: S0017–9310(98)00290–7

χ von-Karmann constant
μ, μ_t laminar and eddy viscosity
ρ density of the fluid
σ_k, σ_ε empirical constant
$\tau_{x,w}$, $\tau_{z,w}$ x-component and z-component of wall shear stress.

Subscripts
e free-stream region
i, j, k tensor index
l, m, n tensor index
p first nodal point adjacent to the wall
w wall.

1. Introduction

Longitudinal vortices have been used to manage separation on aircraft and to control the heat transfer in turbomachinery. For example, in the cases of a plat-fin cross-flow heat exchanger, longitudinal vortices which are induced by each winglet-pair cause the swirling of the flow around the axis parallel to the streamwise direction, and increase the mixing between the external stream and the hot wall, resulting in the high level of heat transfer. In turbomachinery, longitudinal vortices collect and sweep away the protective boundary layer allowing high rates of heat transfer between the hot stream and the surface, damaging the underlying structure. Therefore, a better understanding of the characteristics of heat transfer in a three-dimensional turbulent boundary layer, with longitudinal vortices, is very important in engineering design.

Pearcy [1] developed the design rules to determine the optimum configuration of vortex generators to prevent boundary layer separation. Systematic studies of the flow field have been carried out by Shabaka et al. [2] and Mehta et al. [3]. They investigated the three main cases such as single imbedded vortex, imbedded pair vortex with common flow up and down and found large changes occurring in all the dimensionless structural parameters of turbulent flows and heat transfer. Also, they showed that the structure of heat transfer and turbulent flow with an imbedded vortex pair exhibited a more complex picture than that with a single vortex. Westphal et al. [4] found that the vortex core was observed to have an elliptical shape for downstream due to the presence of the wall. Eibeck et al. [5] have conducted experiments on longitudinal vortices imbedded in a turbulent boundary layer and they concluded that longitudinal vortices are found to influence heat transfer behavior significantly.

With recent advances in computers, the second-moment closure such as a Reynolds Stress Model (RSM) has been widely used in complex flows. While the standard k–ε model provides excellent predictions for many flows of engineering interest, this model cannot predict effectively the anisotropy of turbulent normal stresses in the outer layer with a significant secondary flow because it is based on the Boussinesq eddy-viscosity approximation [6]. However, the feature that, in the second-moment closure, the additional generation terms induced by the secondary flow can be handled exactly should be one of the most attractive advantages when predicting complex flows.

Deb et al. [7] performed the computation of heat transfer and flow structure in a rectangular channel with longitudinal vortices using the standard k–ε model. They concluded that the discrepancies in the distorted region were due to the turbulent model itself and wall-function approach. However, in their work, they did not compare appropriately the results of heat transfer with experimental data.

Hence, in the present study, we use the RSM beyond the Boussinesq approximation and compare results of the RSM with experimental data and results of the standard k–ε model. Wroblewski and Eibeck [8] have conducted the experimental measurement for the turbulent heat transport in the boundary layer with a single vortex. Their results have shown that the heat flux vector and temperature gradient vector align with each other, indicating that the gradient-diffusion model based on the isotropic eddy diffusivity would be suitable for the class of this flow. Hence, in the present calculation, we adopt the simple form of the energy equation which is based on the isotropic eddy-diffusivity model.

The main objectives of this paper are to understand the fundamental mechanism of the turbulent boundary layers with embedded longitudinal vortices and predict the heat transfer characteristics. Also, another purpose is to compare the present results computed by the RSM with the experimental data performed by Pauley and Eaton [9] and the results computed by the standard k–ε model [10]. It can be stated that the RSM can produce a more accurate prediction for capturing the anisotropy than the standard k–ε model. For the thermal boundary layer, the results obtained by the RSM using the eddy-diffusivity model are in slightly better agreement with the experimental data than those by the standard k–ε model using the eddy-diffusivity model. Also, the more elaborate model for the turbulent-scalar-transport term may be required in order to produce a more accurate prediction of the thermal structure.

2. Governing equations

The time averaged continuity, Navier–Stokes equations and Reynolds stresses transport equations for steady and incompressible flow are written as follows. Essentially this is based on the model of Gibson and Launder [11], which incorporates ideas from Rotta [12] and Naot et al. [13]. This version of the model is valid only at sufficiently high Reynolds number.

Continuity equation

$$\frac{\partial U_j}{\partial x_j} = 0 \tag{1}$$

Navier–Stokes equations

$$\rho \frac{\partial}{\partial x_j}(U_j U_i) = -\frac{\partial P}{\partial x_i} + \frac{\partial}{\partial x_j}(2\mu S_{ji} - \rho\overline{u_j' u_i'}) \tag{2}$$

Reynolds-stress-transport equations

$$\frac{\partial}{\partial x_k}(\rho\overline{u_j' u_i'} U_k) = P_{ij} + d_{ij} + \phi_{ij} - \varepsilon_{ij} \tag{3}$$

where

$$P_{ij} = -\left[\overline{u_j' u_i'}\frac{\partial U_i}{\partial x_k} + \overline{u_i' u_j'}\frac{\partial U_i}{\partial x_k}\right] \tag{4}$$

$$d_{ij} = \frac{\partial}{\partial x_k}\left[\frac{c_\mu}{\sigma_k}\frac{k^2}{\varepsilon}\frac{\partial}{\partial x_k}(\overline{u_i' u_j'})\right] \tag{5}$$

$$\varepsilon_{ij} = \frac{2}{3}\delta_{ij}\varepsilon \tag{6}$$

$$\phi_{ij,1} = c_1 \frac{\varepsilon}{k}\left[\overline{u_j' u_i'} - \frac{2}{3}\delta_{ij}k\right] \tag{7}$$

$$\phi_{ij,2} = -c_2\left[P_{ij} - \frac{1}{3}\delta_{ij}\overline{u_l' u_j'}\frac{\partial U_{li}}{\partial x_m}\right] \tag{8}$$

$$\phi_{ij,w} = c_{w1}\frac{\varepsilon}{k}\left[\overline{u_l' u_m'} n_k n_m d_{ij} - \frac{3}{2}\overline{u_k' u_i'} n_k n_j - \frac{3}{2}\overline{u_k' u_j'} n_k n_i\right] f + c_{w2}\frac{\varepsilon}{k}\left[\phi_{km,2} n_k n_m d_{ij} - \frac{3}{2}\phi_{km,2} n_k n_j - \frac{3}{2}\phi_{km,2} n_k n_i\right] f. \tag{9}$$

Energy dissipation equation

$$\rho U_j \frac{\partial \varepsilon}{\partial x_j} = c_{\varepsilon 1}\frac{\varepsilon}{k}\left(-\rho\overline{u_i' u_j'}\frac{\partial U_1}{\partial x_j}\right) - c_{\varepsilon 2}\frac{\rho\varepsilon^2}{k} + \frac{\partial}{\partial x_j}\left(\left(\mu + \frac{\mu_t}{\sigma_\varepsilon}\right)\frac{\partial \varepsilon}{\partial x_j}\right). \tag{10}$$

For temperature field, the energy equation can be written as

$$\frac{\partial}{\partial x_k}(U_k T) = \alpha\nabla^2 T + \frac{\partial}{\partial x_k}(-\overline{u_k' T'}) \tag{11}$$

where,

$$\frac{\dot{q}''_{app}}{\rho} = \frac{\partial}{\partial x_k}(-\overline{u_k' T'}) = \frac{\partial}{\partial x_k}\left(\alpha_t \frac{\partial T}{\partial x_k}\right) \tag{12}$$

where, α_t and $\dot{q}''_{app}$ are the thermal eddy diffusivity and the apparent heat flux respectively.

The empirical coefficients appearing in the above equations are summarized in Table 1.

Table 1
Turbulence model constants

c_μ	c_1	c_2	c_{w1}	c_{w2}	$c_{\varepsilon 1}$	$c_{\varepsilon 2}$	σ_k	σ_ε
0.09	1.8	0.6	0.5	0.3	1.44	1.92	1.0	1.3

3. Numerical approach and boundary conditions

The governing equations without boundary layer simplifications are solved by a finite volume method on a staggered grid system, with scalar quantities being stored at the center of the scalar control volume and all other quantities stored at the cell faces as shown in Fig. 1. In order to provide the pressure field, the SIMPLE scheme is adopted in the present solution procedure.

3.1. Inlet conditions

The inlet boundary conditions for velocity and temperature can be specified using the profiles extracted from the experiment [9]. However, for turbulent stresses, the experimental data are so deficient that we cannot directly use the profiles of turbulent stresses from experimental data. Hence, the turbulent stresses and dissipation are calculated from velocities in the inlet region. As shown in Fig. 2(a), the south, top and bottom faces are treated as the wall except for the north face which is the symmetric condition. For the wall boundary, a possible approach to resolve the region $y^+ < 50$ is to use a low-Reynolds-number model, but this approach is too costly in general 3D flows. The alternative is to adopt the wall-function approach. In the present calculation, the wall functions are used to bridge the near wall region as follows.

$$\tau_{x,w} = \frac{c_\mu^{1/4} k_P \chi U_P}{\ln(Ey^+)}, \quad \tau_{z,w} = \frac{c_\mu^{1/4} k_P \chi W_P}{\ln(Ey^+)} \tag{13}$$

where y_P^+ is redefined as

$$y_P^+ = \frac{\rho c_\mu^{1/4} k_P^{1/2} y_P}{\mu}, \tag{14}$$

$\chi = 0.42$ which is known as von Karmann constant. The subscript p refers to the first nodal point adjacent to the wall. In fact, the steep gradients of both mean-flow and turbulence quantities also necessitate modification to the turbulence transport equations. The present approach is based on the two-layers methodology, details of which may be found in Launder [14].

At the wall, in order to apply the wall function for temperature, the heat flux at the wall can be expressed as

$$\dot{q}''_{app} = \frac{\rho c_\mu^{1/4} k_p^{1/2} c_p (T_w - T_P)}{T_P^+} \tag{15}$$

where T_P^+ may be written as

$$T_P^+ = Pr_t[U_P^+ + P_{fn}]. \tag{16}$$

It may be mentioned that P_{fn} in equation (24) is the Pee function which may be written as [15]

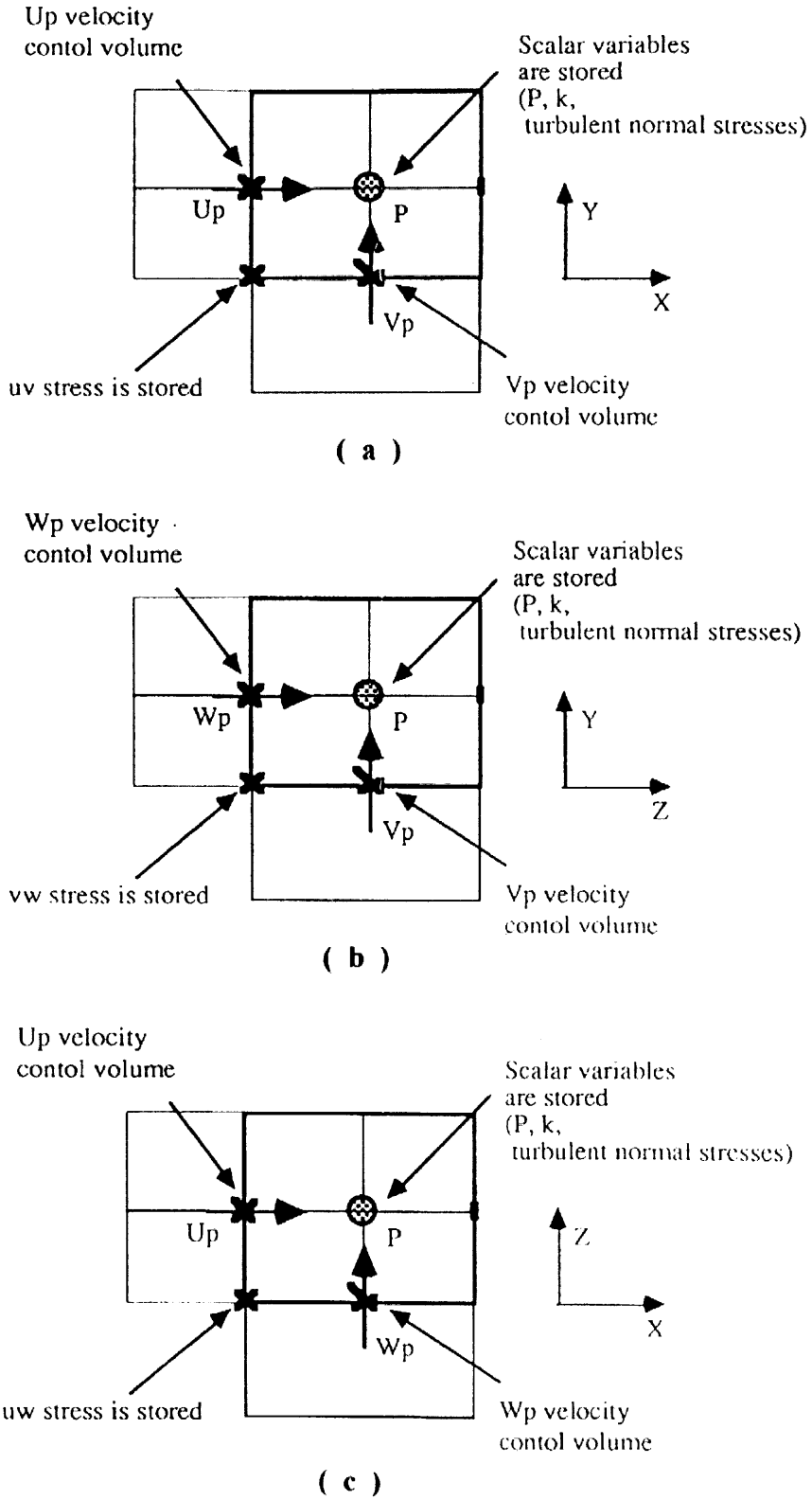

Fig. 1. Staggered velocity/stress arrangement: (a) x–y cross section; (b) y–z cross section; (c) x–z cross section.

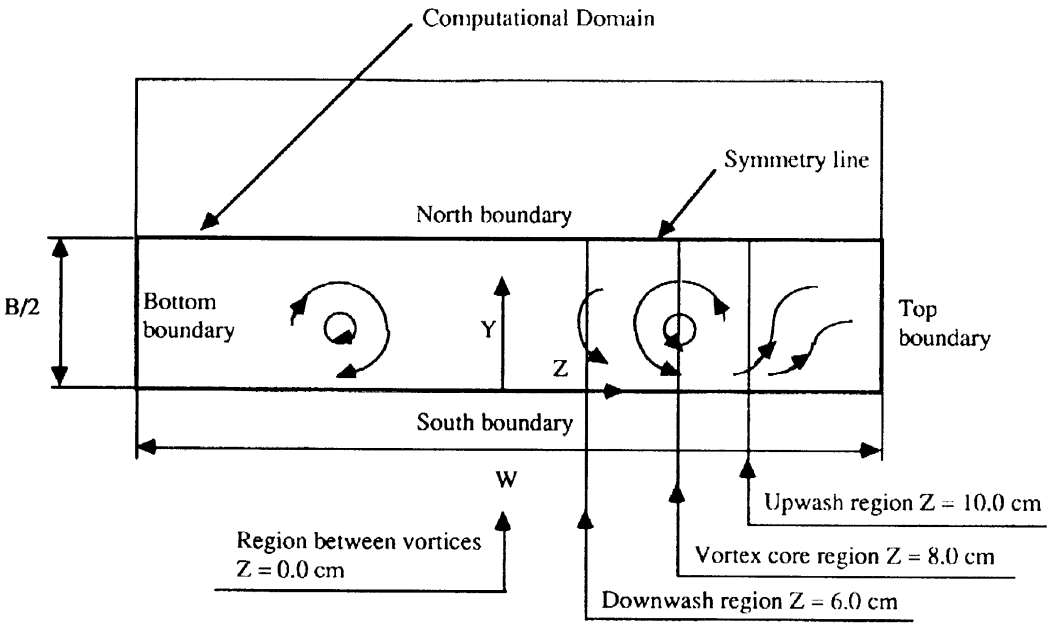

(a)

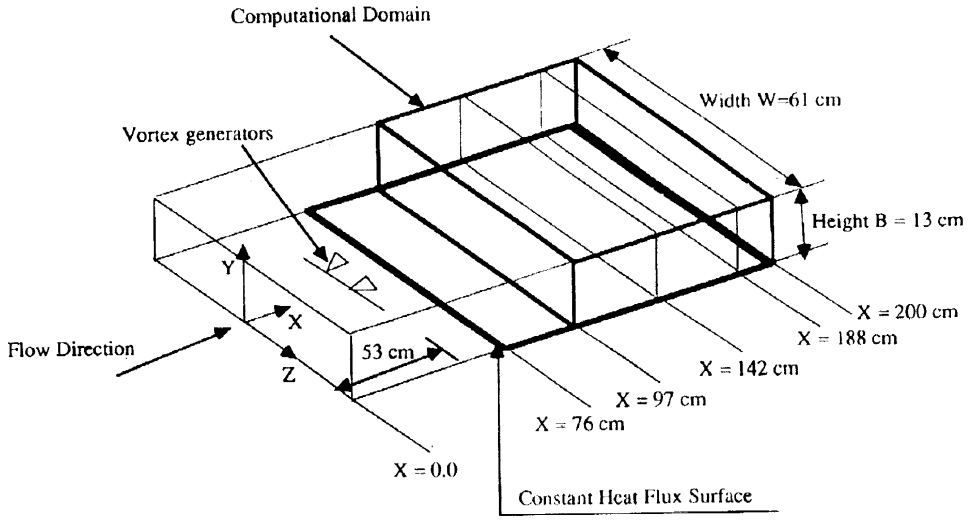

(b)

Fig. 2. (a) Cross-section of the computational domain; (b) schematic of the experimental facility of Pauley and Eaton [9].

$$P_{\mathrm{fn}} = 9.24\left[\left(\frac{Pr}{Pr_{\mathrm{t}}}\right)^{3/4} - 1\right]\cdot\left[1 + 0.28 \cdot \exp\left(-0.007\cdot\left(\frac{Pr}{Pr_{\mathrm{t}}}\right)\right)\right]. \quad (17)$$

4. Numerical results and discussions

The experimental facility of Pauley and Eaton [9] is shown in Fig. 2(b). They have conducted measurements at four cross sections, namely, $x = 66$, 97, 142 and 188 cm. As seen in this figure, the turbulent boundary layer is affected by longitudinal pair vortices which are generated by delta wings, and heated by the constant heat flux surface from the position at $x = 76$ cm. This facility has 200 cm long test section with a 13×61 cm cross section and is operated at a normal free-steam velocity of 16 m s^{-1}. Also, Reynolds number based on the half height of the channel, $Re_{B/2}$, is adopted as 67 000 from the experimental data. In this calculation, Prandtl number and turbulent Prandtl number are used as 0.7 and 0.9 respectively. In the real experimental situation, thermal boundary layer begins at $x = 76$ cm downstream. But, in the present study, the cross-section at $x = 97$ cm is selected as the inlet plane because there is no obvious information for the initial conditions at $x = 76$ cm downstream. In this study, the measured data in ref. [9] for velocity, turbulent normal stresses and temperature at $x = 97$ cm are used as inlet profiles for the computational domain by interpolation. The constant heat flux at the wall and the temperature difference between the wall and freestream are the same as the experimental conditions. That is, the constant wall heat flux and temperature difference, namely, $\dot{q}''_{\mathrm{w}}$ and ΔT are taken as 817 W m^{-2} and 20°C respectively in the present calculation. Comparisons of the predictions given by the RSM and the standard k–ε model with experimental data are accomplished at $x = 142$ and $x = 188$ cm downstream. In the case of the RSM, the computing time for convergence is about 4 h using the CRAY-YMP computer. All the results of the standard k–ε model for the present comparison are taken from the previous study conducted by Jeong and Ryou [10].

Figure 3 shows the grid system ($35 \times 35 \times 58$: X, Y and Z) with concentration of grid points in the south wall region. However, as shown in this figure, a coarse meshsize in the top and bottom wall is used to reduce the sidewall effect possibly.

4.1. Mean and turbulent structure

Contours of the streamwise velocity calculated by the RSM are compared with experimental data at two different planes shown in Fig. 4. It can be indicated that the strong distortion of the boundary layer caused by the vortices. At each axial station the outermost edge illustrates the undisturbed boundary layer. The boundary layer is thickened markedly in the upwash region where the vortex sweeps low momentum fluid away from the wall. In the downwash region the boundary layer is thinned by the strong downflow and lateral outflow of boundary layer fluid. As shown in this figure, reasonably good agreement is seen between the experimental data and the calculated results. But, at $x = 188$ cm downstream, it is seen that the RSM overpredicts the diffusion of vortical flows.

Figure 5 which presents the comparison of the secondary velocity vectors given by the RSM with experimental data indicates the process of vortex motion as follows: if a vortex suffers the perturbation which causes the static pressure on the axis to rise, the axial velocity near the vortex axis will decrease, hence there will be a radial outflow to satisfy the continuity equation, and the vortex diameter will thus increase slightly, approximately conserving angular momentum, so that the angular velocity at the given radius decreases. The process continues until the vortex is stable with a new and large diameter, the same circulation, and thus a lower angular velocity or vorticity. However, at $x = 188$ cm downstream, it is observed that the secondary velocities computed by the RSM have more diffused shape than those obtained from the experiment.

The skin friction coefficients calculated by using the RSM and the standard k–ε model are compared with the experimental data at $x = 142$ and 188 cm downstream as shown in Fig. 6. In a whole region, c_{f} predicted by the RSM are underpredicted by maximum error of 7% as compared with the experimental data. In the upwash and downwash region, the RSM shows the better performance to predict the skin friction coefficient than the standard k–ε model. However, in the vortex core region at $x = 188$ cm, the calculated values of the standard k–ε model are rather slightly closer to the experimental data than those predicted by using the RSM. This may be because the RSM produces inaccurate prediction of the vortex diffusion in the vortex core region. Nevertheless, the remarkable differences between both models are not observed.

Figures 7–9 show the comparisons of the turbulent normal stresses computed by using both models with the experimental data in the downwash region ($z = 6$ cm), vortex core region ($z = 8.0$ cm) and upwash region ($z = 10.0$ cm) at $x = 188$ cm downstream. As expected, it can be seen that the RSM can capture an anisotropy of turbulence effectively, but the standard k–ε model fails to predict an anisotropy in these regions because the standard k–ε model is intrinsically based on the isotropic concept. In particular, from the turbulent normal stress profiles in the downwash and upwash region, we can see that in the vicinity of wall, the RSM produces the more

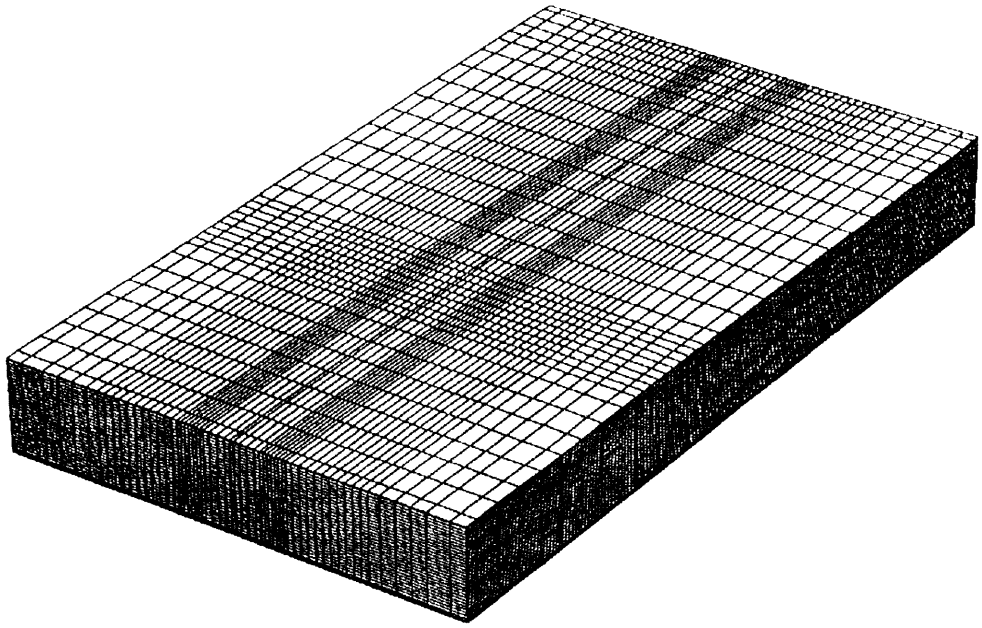

Fig. 3. Grid generation ($35 \times 35 \times 58$: X, Y and Z).

accurate prediction than the standard k–ε model. On the other hand, in the vortex core region, in the results predicted by the RSM severely deviate from the experimental data in the outer layer and vortex center. These results may be because the RSM yields too strong anisotropy. That is, even in the isotropic region, it may be thought that the RSM compels the turbulent normal stresses to be anisotropic. This is due to shortcomings of the RSM itself. On the whole, a high level of turbulent normal stresses are observed in the vicinity of the wall, but a reduced level of turbulent kinetic energy found in the vortex center and in the tongue of fluid extending from the wall in the upwash region. This accompanies the diffusion of the velocity which is presented in the vortex core at the upstream. In addition, the energy level in the upwash region is reduced. The likely explanation is that because the secondary flow is much weaker than that of the upstream location, so it is less able to convect the high energy fluid from near the wall outward before the turbulent energy can be diffused in the tongue of fluid in the upstream region.

4.2. Thermal boundary layer structure

The main focus of this study is to compare the results calculated by the RSM and the standard k–ε model using the identical eddy-diffusivity model for the thermal boundary layer. That is, it is a matter of primary concern to show how the effective prediction for turbulent flows affects the thermal boundary layer.

The notation of the RSM shown in the following figures represents the case of the RSM for the turbulent calculation using the eddy-diffusivity model for the thermal boundary layer. Figure 10 shows the comparisons of the normalized temperature profile for the selected spanwise locations at $x = 188$ cm downstream. These locations represent the regions between vortices ($z = 0.0$ cm), downwash region ($z = 6.0$ cm), vortex core ($z = 8.0$ cm) and upwash region ($z = 10.0$ cm) respectively as shown in Fig. 3. The thermal boundary layer is thinned between the vortices and thickened in the upwash region where the secondary flow is directed away from the wall. The calculated results are in good agreement with the experimental data. However, this figure shows that the temperature profiles in the region of vortex core ($z = 8.0$ cm) slightly deviate from the experimental data. This discrepancy may be due to the immoderate overprediction of the vortex diffusion in the core region. However, as indicated in the analysis of the previous section, the results of the RSM showed better agreement with experimental data than those of the standard k–ε model in the downwash and upwash regions. In particular, in the upwash region, the RSM is very good. However, in the center of vortex, we can observe that the temperature profiles computed by the RSM severely deviate from the experimental data except near the wall. Probably, this discrepancy results from the inaccurate prediction of turbulent flows in the core region.

On the whole, it is interesting that the results computed by RSM are closer to experimental data near the wall than the remote region away from the wall. The likely explanation is that the RSM can capture the anisotropy

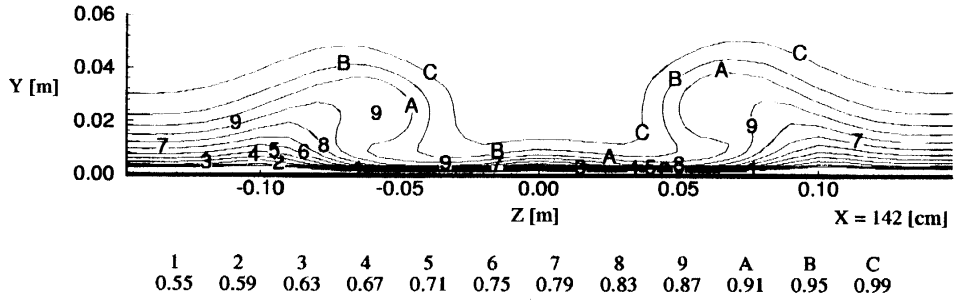

(a)

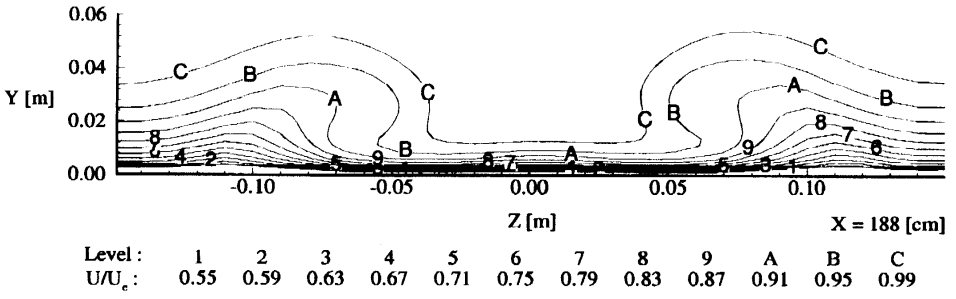

(b)

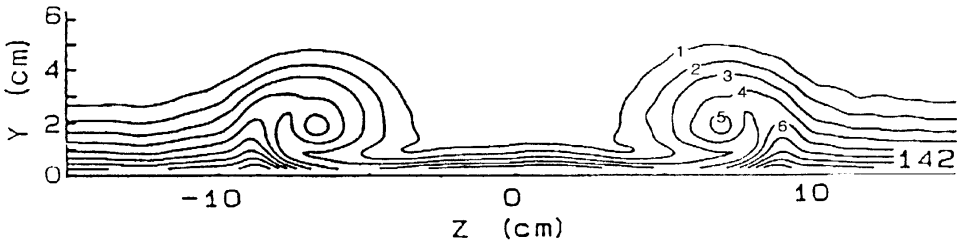

Level : 1 2 3 4 5 6

U/U$_e$: 0.99 0.95 0.90 0.85 0.80 0.75

(c)

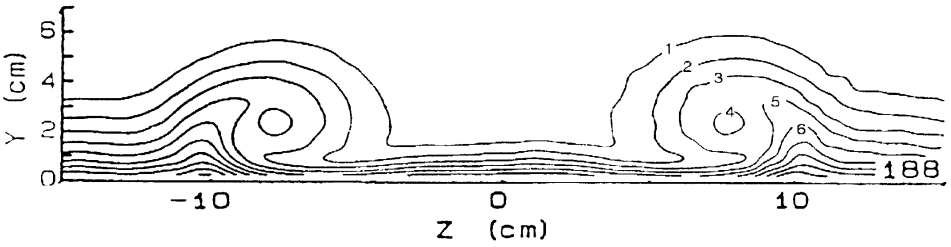

Level : 1 2 3 4 5 6

U/U$_e$: 0.99 0.95 0.90 0.85 0.80 0.75

(d)

Fig. 4. Comparisons of the streamwise velocity: (a) RSM at $x = 142$ cm downstream; (b) RSM at $x = 188$ cm downstream; (c) experiment at $x = 142$ cm downstream; (d) experiment at $x = 188$ cm downstream.

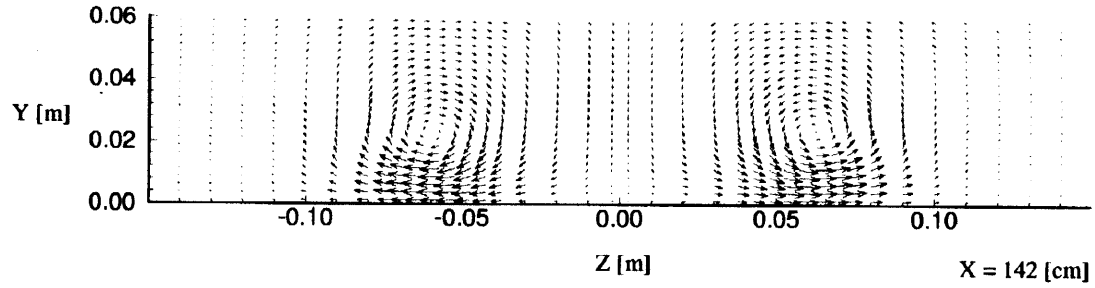

(a)

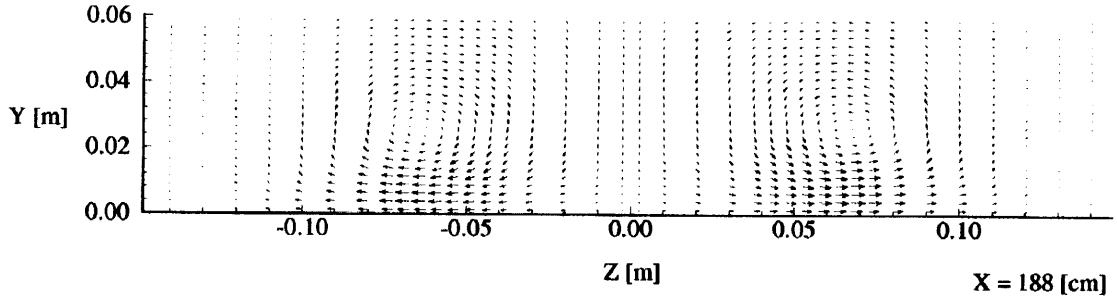

(b)

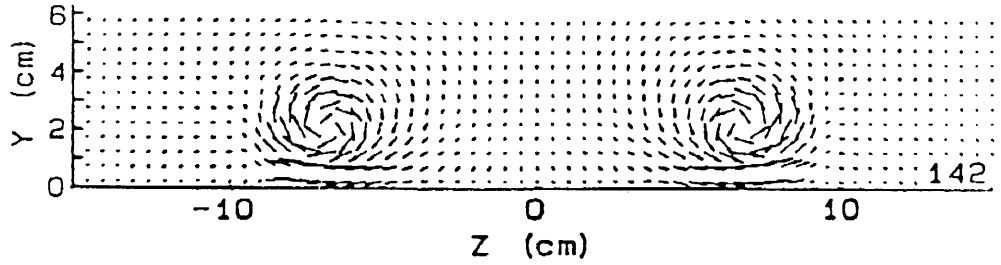

(c)

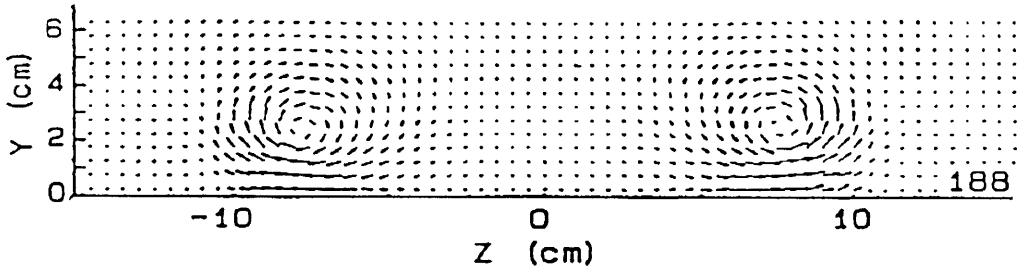

(d)

Fig. 5. Comparisons of the secondary velocity vectors: (a) RSM at $x = 142$ cm downstream; (b) RSM at $x = 188$ cm downstream; (c) experiment at $x = 142$ cm downstream; (d) experiment at $x = 188$ cm downstream.

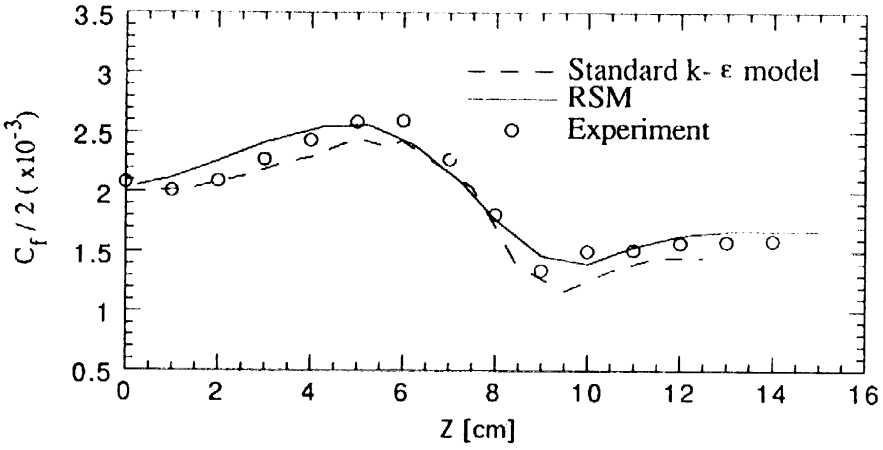

(a)

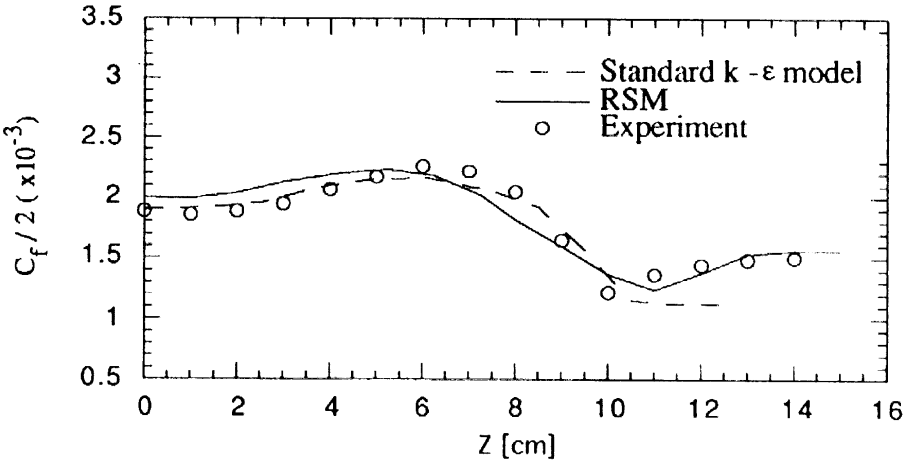

(b)

Fig. 6. Comparisons of skin friction coefficient at $x = 142$ and 188 cm: (a) $x = 142$ cm; (b) $x = 188$ cm.

of the turbulent normal stresses because there is a strong anisotropy of turbulent structure in the vicinity of the wall. Therefore, we can see from these results that the accurate prediction of turbulent flows is very important for prediction of temperature fields.

Figure 11 indicates that the local Stanton number obtained by both models at $x = 142$ and $x = 188$ cm are compared with the experimental data. It is noted from these figures that the heat transfer in the undisturbed region is less enhanced than the region which is affected by secondary flow. And it can be noted that the vortex core is a region of relatively lower mixing than the downwash region. Also, the peak value calculated by using the RSM is found in the downwash region. It is seen that this peak value in the downwash region is greater than the minimum Stanton number found in the upwash region by about 36.9%. In a whole region, the results calculated by the RSM produce slightly better prediction than those given by the standard k–ε model although there are considerable differences compared to experimental data for

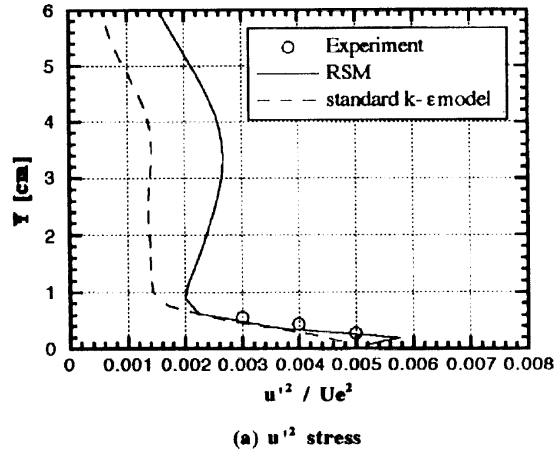

(a) u'^2 stress

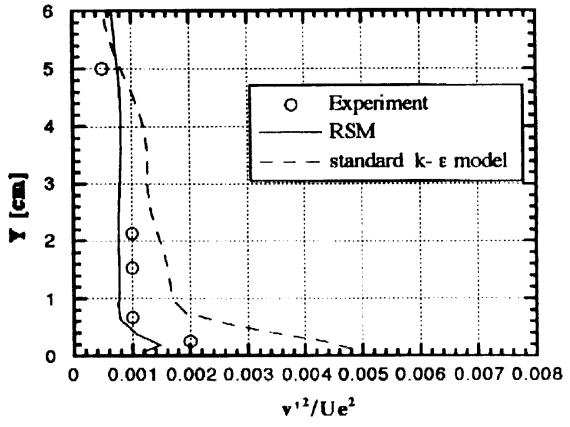

(b) v'^2 stress

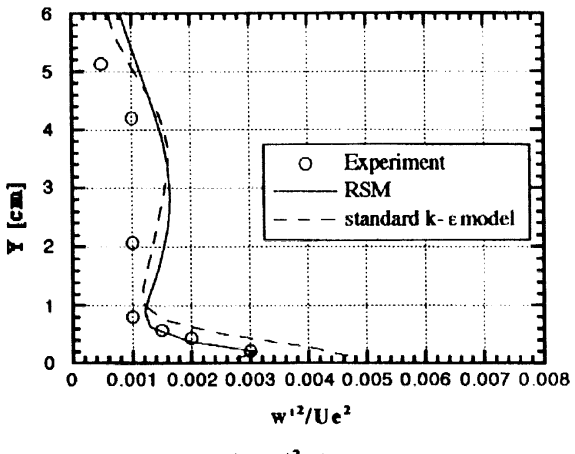

(c) w'^2 stress

Fig. 7. Comparisons of Reynolds normal stresses in the downwash region at $x = 188$ cm.

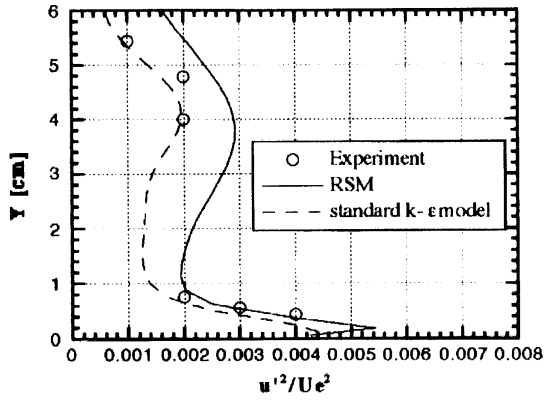

(a) u'^2 stress

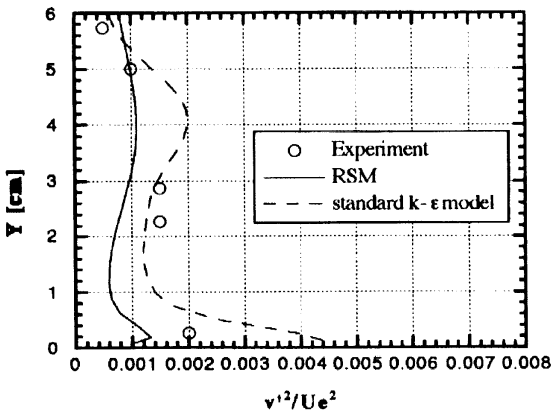

(b) v'^2 stress

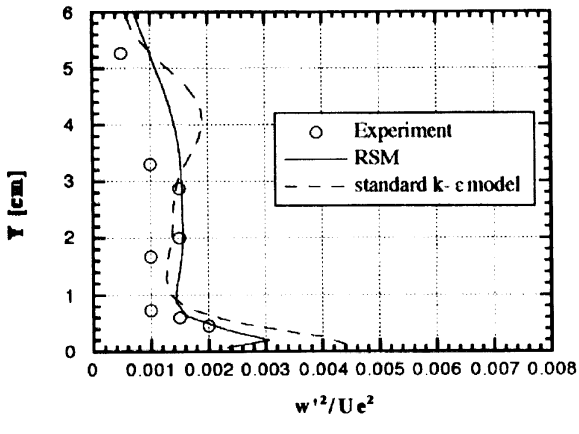

(c) w'^2 stress

Fig. 8. Comparisons of Reynolds normal stresses in the vortex core region at $x = 188$ cm.

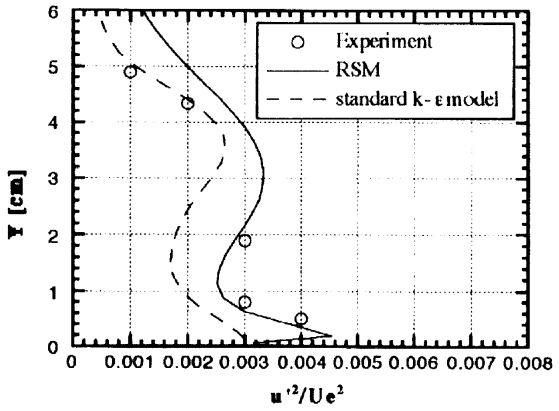

(a) u'^2 stress

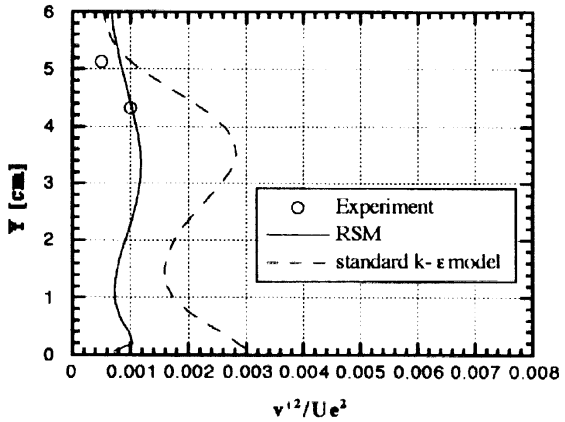

(b) v'^2 stress

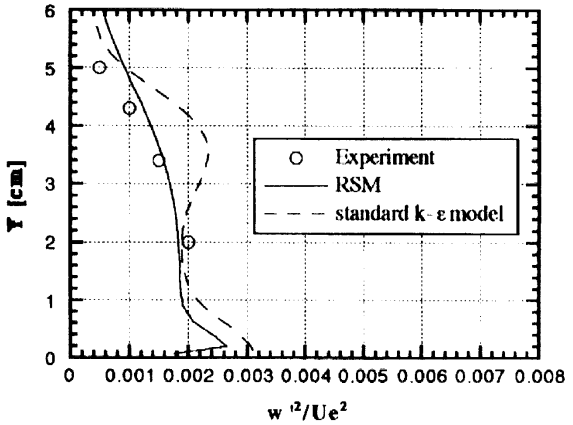

(c) w'^2 stress

Fig. 9. Comparisons of Reynolds normal stresses in the upwash region at $x = 188$ cm.

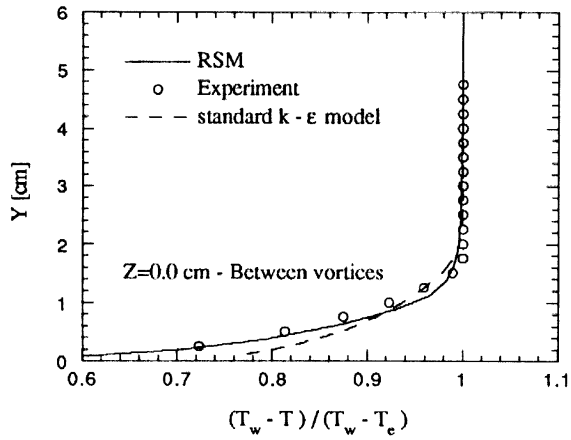

(a) Between vortices (Z = 0.0 cm)

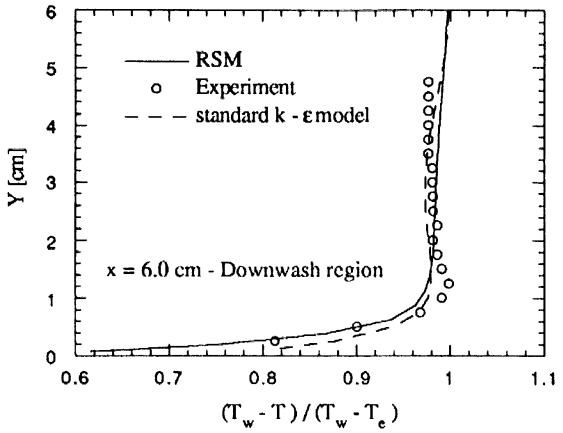

(b) Downwash region (Z = 6.0 cm)

Fig. 10. Comparisons of normalized temperature profiles at $x = 188$ cm: (a) between vortices ($z = 0.0$ cm); (b) downwash region ($z = 6.0$ cm); (c) vortex core region ($z = 8.0$ cm); (d) upwash region ($z = 10.0$ cm).

both models due to the eddy-diffusivity model. Hence, it may be thought that a more elaborate model for turbulent-scalar-transport terms such as the second-moment-closure model is needed to produce better prediction for the thermal boundary layer.

5. Conclusions

We can conclude that the RSM can produce more accurate predictions to capture anisotropy of the tur-

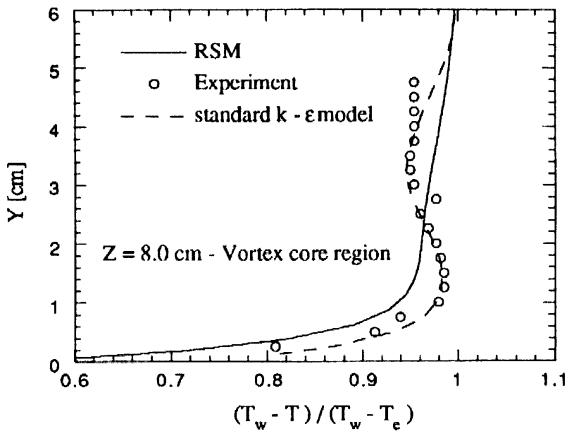

(c) Vortex core region (Z = 8.0 cm)

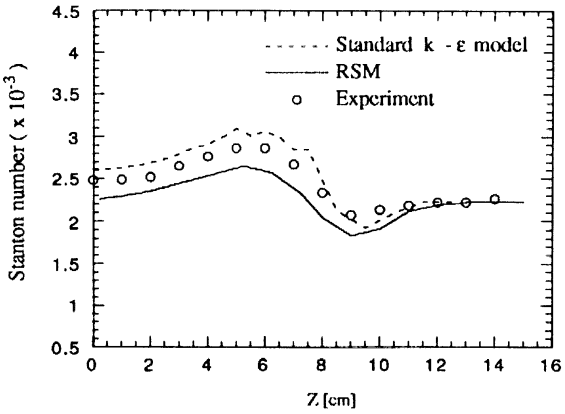

(a) Stanton number at X = 142 cm

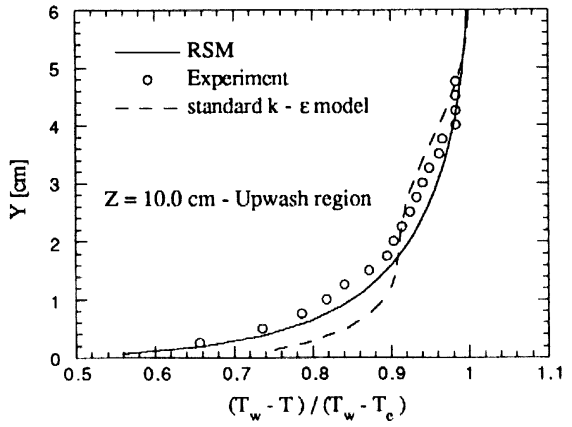

(d) Upwash region (Z = 10.0 cm)

Fig. 10. *Continued.*

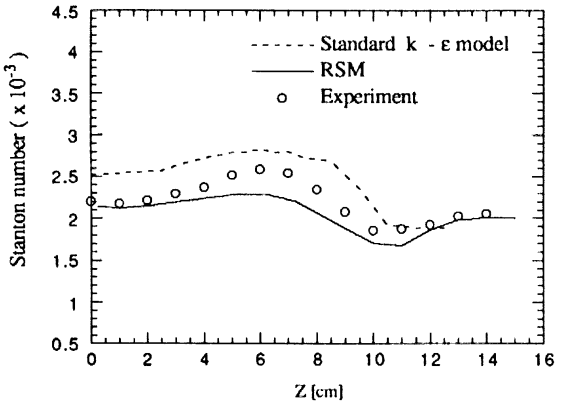

(b) Stanton number at X = 188 cm

Fig. 11. Comparisons of local Stanton number at 142 and 188 cm: (a) $x = 142$ cm; (b) $x = 188$ cm.

bulent intensities than the standard k–ε model. Also, it can be seen that except in the vortex core region, the RSM gives better predictions of the turbulent normal stresses and temperature distributions in the vicinity of the wall than the standard k–ε model. However, the strong anisotropy tendency is shown at the core region. This may be due to the inappropriate modeling of the pressure-strain correlation term.

For the thermal boundary layer, the results of this study indicate that the disturbance of the boundary layer causes the highest level of Stanton number in the region where the flows are directed toward the wall, but the vortex core is the region of relatively lower mixing. On the whole, the present results obtained by the RSM using the eddy-diffusivity model are in slightly better agreement with the experimental data than those by the standard k–ε model. However, the considerable differences cannot be found for both models due to the identical eddy-diffusivity model for thermal boundary layer. This indicates that more elaborate consideration for the turbulent-scalar-transport model may be needed in order to produce better prediction for the thermal boundary layer.

Acknowledgements

This work is supported by the Korea Science and Engineering Foundation (KOSEF) through the TPMRC at Seoul National University and Korea Ministry of Edu-

cation through Mechanical Engineering Research Fund (ME95-B-10).

References

[1] H.H. Pearcy, Boundary Layer and Flow Control, G.V. Lachmann, (Ed.), vol. IV, 1961.
[2] I.M.M.A. Shabaka, R.D. Mehta, P. Bradshaw, Longitudinal vortices imbedded in turbulent boundary layers—Part 1: single vortex, J. Fluid Mech. 155 (1985) 37–57.
[3] R.D. Mehta, P. Bradshaw, Longitudinal vortices imbedded in turbulent boundary layers, J. Fluid Mech. 188 (1988) 529–546.
[4] R.V. Westphal, J.K. Eaton, W.R. Pauley, Interaction between a vortex and a turbulent boundary layer in a streamwise pressure gradient, Turbulent Shear Flows 5, Springer-Verlag, vol. III, 1987, pp. 266–277.
[5] P.A. Eibeck, J.K. Eaton, Heat transfer effects of a longitudinal vortex imbedded in a turbulent boundary layer, J. Heat Transfer 109 (1987) 16–24.
[6] D.C. Wilcox, Turbulence Modeling for CFD, DCW Industries Inc., Lacanada, CA, 1993, pp. 213–218.
[7] P. Deb, G. Biswas, Heat transfer and flow structure in laminar and turbulent flows in a rectangular channel with longitudinal vortices Int. J. Heat Mass Transfer 38 (13) (1995) 2427–2444.
[8] D.E. Wroblewski, P.A. Eibeck, Measurements of turbulent heat transport in a boundary layer with an embedded streamwise vortex, Int. J. Heat Mass Transfer 34 (7) (1991) 1617–1631.
[9] W.R. Pauley, J.K. Eaton, The fluid dynamics and heat transfer effects of streamwise vortices embedded in a turbulent boundary layer, Report MD-51, Department of Mechanical Engineering, Stanford University, 1988.
[10] J.Y. Jeong, H.S. Ryou, Numerical simulation of heat transfer and flow structure in 3-D turbulent boundary layer with imbedded longitudinal vortex, Num. Heat Transfer A 31 (1997) 433–450.
[11] M.M. Gibson, B.E. Launder, Ground effects on pressure fluctuations in the atmospheric boundary layer, J. Fluid Mech. 86 (1978) 491–511.
[12] J.C. Rotta, Statistische theorie nichthomogener turbulenz, Zeitschrift fur Phisik 129 (1951) 548–572.
[13] D. Naot, A. Schavit, M. Wolfshtein, Interaction between components of the turbulent velocity correlation tensor, Israel J. Tech 8 (1970) 259.
[14] B.E. Launder, Low-Reynolds-number turbulence near walls, Report TFD/86/4, Department of Mechanical Engineering, UMIST, 1986.
[15] C.L. Jayatilleke, The influence of Prandtl number and surface roughness on the resistance of the laminar sublayer to momentum and heat transfer, Prog. Heat Mass Transfer 1 (1969) 193–329.